Soft Matter

Three-Dimensional Thermochromic LCE Structures with Reversible Shape-Morphing and Color-Changing Capabilities for Soft Robotics

Journal:	*Soft Matter*
Manuscript ID	SM-ART-06-2022-000876.R1
Article Type:	Paper
Date Submitted by the Author:	11-Aug-2022
Complete List of Authors:	Li, Yi; University of Connecticut, Materials Science and Engineering Teixeira, Yasmin; University of Connecticut Parlato, Gina; University of Connecticut Grace, Jaclyn; University of Connecticut Wang, Fei; University of Connecticut Huey, Bryan; University of Connecticut Wang, Xueju; University of Connecticut, Materials Science and Engineering

Title: Three-Dimensional Thermochromic LCE Structures with Reversible Shape-Morphing and Color-Changing Capabilities for Soft Robotics

*Yi Li, Yasmin Teixeira, Gina Parlato, Jaclyn Grace, Fei Wang, Bryan D. Huey, Xueju Wang**

[*] Prof. Xueju Wang, corresponding author
Department of Materials Science and Engineering, Institute of Materials Science,
University of Connecticut,
Storrs, CT 06269, USA
Email: xueju.wang@uconn.edu

Yi Li, Gina Parlato, Jaclyn Grace, Fei Wang, and Prof. Bryan D. Huey
Department of Materials Science and Engineering,
University of Connecticut,
Storrs, CT 06269, USA

Yasmin Teixeira
Polymer Program, Institute of Materials Science,
University of Connecticut,
Storrs, CT 06269, USA

Keywords: reversible shape morphing, color-changing, camouflage, liquid crystal elastomers, soft robots

Abstract

Functional structures with reversible shape-morphing and color-changing capabilities are promising for applications including soft robotics and biomimetic camouflage devices. Despite extensive studies, there are few reports on achieving both reversible shape-switching and color-changing capabilities within one structure. Here, we report a facile and versatile strategy to realize such capabilities via spatially programmed liquid crystal elastomer (LCE) structures incorporated with thermochromic dyes. By coupling the shape-changing behavior of LCEs resulting from the nematic-to-isotropic transition of liquid crystals with the color-changing thermochromic dyes, 3D thermochromic LCE structures change their shapes and colors simultaneously, which are controlled by the nematic-isotropic transition temperature of LCEs and the critical color-changing temperature of dyes, respectively. Demonstrations, including the simulated blooming process of a resembled flower, the camouflage behavior of a "butterfly"/"chameleon" robot in response to environmental changes, and the underwater camouflage of an "octopus" robot, highlight the reliability of this strategy. Furthermore, integrating micro-ferromagnetic particles into the "octopus" thermochromic LCE robot allows it to respond to external magnetic fields for diverse biomimetic motion modes, including swimming, rolling, slippage, rotating and crawling, accompanied by color-changing behaviors. The reversibly reconfigurable and color-changing thermochromic LCE structures are promising for applications including soft camouflage/reconnaissance robots and multifunctional bionic devices.

1. Introduction

Functional structures with synchronous shape-morphing and color-changing capabilities are promising for many applications, including soft robotics, biomimetic camouflage devices, and many others. Take camouflage for example, living organisms, such as fish and cephalopods, generally realize it through introducing a rich variety of colors, vivid geometrical and random patterns, and morphological structures (morphing), which assist the animal to avoid detection from predators[1-4]. Mimicking camouflage capabilities in nature is promising for potential applications including in advanced biomimetic devices[5], electronic skins[5-7] and soft robotics[8-11]. Artificial camouflage usually relies on dye or pigment colors and structural colors for background matching and breaking coloration[12-14]. For example, camouflage objects selectively express or destroy various patterns/hues to match the background via changing the refraction of light (visible, 400-700 nm wavelength)[15, 16], thermal absorption[17, 18], and pigment precipitation[19]. Recently, a thermochromic liquid crystal layer with vertically stacked, patterned silver nanowire heaters has been used to retrieve the local background color and matches its surface color instantaneously with natural transition characteristics, which overcomes the limitations of traditional lateral pixelation schemes[20]. Furthermore, pneumatically inflating thin membranes of main-chain chiral nematic liquid crystalline elastomers (LCEs) is used to achieve pixelated structural coloration with broadband spectral shifts in a compact space[21].

Camouflage behaviors of many creatures such as octopuses in nature are usually accompanied by complex shape morphing[2, 22, 23]. Integrating geometric reconfiguration into color-changing is promising for achieving the fully adaptive artificial camouflage of biomimetic structures and robots. LCEs are a unique class of materials that combine rubber elasticity with the orientational order of liquid crystals (LCs). The coupling between the alignment of LC

molecules and the macroscopic deformation of polymer networks gives rise to unique properties including soft elasticity, large reversible shape changes in response to a stimulus (e.g., heat or light)[24-40], which are promising for a wide range of applications including artificial muscles[41-43], soft robotics[44-47], micromachines[48-50] and biomimetic devices[51-54]. For example, Cai et al.[26] reported a LCE-based soft wireless tubular actuator that can achieve "grabbing cargo" and "motion" modes. In addition, a remotely controlled bioinspired underwater robot reported by Shahsavan H. et al.[55] demonstrates the potential application of LCEs in biomimetic robotics. More recently, we developed a ferromagnetic soft robot with multiple biomimetic motion modes[56], especially passing through a narrow crack under magnetic and thermal stimuli, which highlights the integration of multi-stimuli in the 3D LCE structure for applications in multifunctional soft robotics.

In this work, we develop a facile strategy to enable simultaneous shape-morphing and color-changing capabilities by assembling 3D structures from shape-morphing LCEs embedded with thermochromic dyes. The temperature-induced color change in thermochromic dyes occurs due to the molecular rearrangement of color formers (leuco dyes) in the presence of a developer, the process of which is controlled by a phase change of the co-solvent[57, 58]. Adding thermochromic dyes to LCEs has shown no influence on their mechanical properties and shape-morphing behaviors[59]. Structures including a biomimetic "flower", "butterfly", and "chameleon" exhibit simultaneous reversible shape-morphing and color-changing behaviors when the environment temperature reaches the corresponding critical transition temperature for LCEs and thermochromic dyes. In addition, this strategy can be extended to biomimetic underwater robots, which is demonstrated by the camouflage behavior of "octopus". Furthermore, integrating micro-ferromagnetic particles into thermochromic LCEs enables the magnetic actuation of the robot for

diverse biomimetic motion modes, including swimming, rolling, slippage, rotating, and crawling, accompanied by color-changing behaviors. Such demonstrations present potential applications for the new generation of soft camouflage/reconnaissance robots and multifunctional biomimetic devices.

2. Results and Discussion

2.1 Reconfigurable color-changing thermochromic LCE structures

The schematic diagram in **Figure 1A** shows the reversible shape-morphing and color-changing behavior of 3D thermochromic LCE mesostructures assembled via tensile buckling. The strategy starts with the synthesis of thermochromic LCEs, which follows the two-stage thiol–acrylate Michael addition reaction (TAMAP) methodology[60]. The structural component, 4-bis-[4-(3-acryloyloxypropypropyloxy) benzoyloxy]-2-methylbenzene (RM257), the crosslinker, (2,2-(ethylenedioxy) diethanethiol (EDDET), and the monomer, pentaerythritol tetrakis(3-mercaptopropionate) (PETMP), are mixed to form an intermediate polydomain LCE network. Subsequently, adding the photoinitiator (2-hydroxyethoxy)-2-methylpropiophenone (HHMP) allows for the photopolymerization process in the second reaction stage. To enable the color-changing capability, thermochromic dyes are further mixed thoroughly to the solution, which is then molded into a thermochromic LCE film and patterned into desired 2D geometries using a CO_2 laser (VLS 2.30, University Laser System, Norman, CT). The 2D thermochromic LCE pattern is then transferred onto a silicone elastomer substrate (Dragon Skin, Smooth-on, Easton, PA). Strong adhesion is created at selective locations (bonding sites) between the 2D pattern and the substrate through applying an ultra-thin layer of superglue, while the interface of other locations has relatively weak adhesion dominated by van der Waals forces. Stretching the

elastomer substrate induces forces at the bonding sites and in- and out-of-plane translations of the structure, buckling the 2D thermochromic LCE pattern into a 3D structure. Governed by the compressive strains, mesogens and polymer chains of the LCE structure are spatially aligned[56]. The buckled 3D thermochromic LCE structure is then exposed to ultraviolet (UV) light (wavelength: 365-400 nm), completing the second-stage polymerization process, which permanently programs the ordered phase (nematic state) and "locks" the buckled 3D shape of the structure. Removing the 3D thermochromic LCE structure from the substrate accesses the freestanding format of the structure. By heating and cooling across the isotropic clearance temperature[32] of LCEs, a nematic-to-isotropic transition can be reversibly achieved, thereby enabling the reversible macroscopic 3D-2D shape transformation of the structure. In addition to large and reversible shape-morphing behaviors[56], the 3D thermochromic LCE structure is endowed with unique color-changing capabilities upon temperature changes, which will be discussed in details in the following.

Thermochromic dyes are generally composed of organic leuco-dye mixtures formed by a color former (leuco dye, electron donor), a color developer (usually a weak acid, electron acceptor), and a low-melting organic solvent. Thermochromism arises from the change in the interaction of the leuco dye with the developer in the presence of the solvent. The solvent is a phase-changing material (PCM), which can be a ketone, ether, ester, acid, or long-chain alkyl alcohol[59]. The solvent in each thermochromic dye has its own melting temperature, which determines the critical color-changing temperature of the dye. At temperatures below the melting point of the solvent, electron interaction between the color former and the color developer, which are in contact, induces a visible color. Heating above the melting temperature of the solvent

dissolves the solvent and causes the separation of the color former and the color developer, and therefore the loss of the color[57, 61, 62].

As shown in **Figure 1B** and **1C**, the flower-like structure changes its color from red to colorless when being heated above 52 ℃ due to the thermochromic properties, and morphs from its 3D to 2D configuration when the temperature further increases above 62 ℃ because of the nematic-to-isotropic state transition[56]. Conversely, cooling the structure below the isotropic clearance temperature of LCEs and the melting point of the solvent preset in the thermochromic dye, the structure reverts to the original red color and recovers from the 2D state to 3D shape. Please note that both the color-changing and shape-morphing behaviors are reversible. Therefore, the flower-like thermochromic LCE structure can exhibit simultaneous reversible shape-morphing and color-changing behaviors under thermal actuation, which resembles a flower at different blooming stages[63, 64] (**Movie S1**).

2.2 Characterization of color-changing thermochromic dyes

The reversible shape-morphing and color-changing behaviors of 3D thermochromic LCE structures discussed above can be accompanied with a variety of color transitions by tuning the types of thermochromic dyes. **Figure 2A** presents experimental characterizations of the color-changing temperature of thermochromic LCE films embedded with different thermochromic dyes: (a) black-colorless, (b) blue-violet, (c) black-green, and (d) red-colorless. Here black-colorless means the dye changes from black to colorless above the melting temperature of the solvent. This definition applies to the other dyes throughout this work. The critical temperatures for the color changes of these dyes are evaluated by submerging the samples in a water bath, where the water temperature is well controlled. The results in Figure 2A show that each

thermochromic dye exhibits three color regions: a low-temperature color region, a transition region, and a high-temperature color region. The bar chart in Figure 2A contains these three color regions separated by two boundary temperatures: a lower temperature indicating when the color starts to change and a higher temperature above which the final color is obtained. Take the blue-violet (b) sample for example, when the temperature is below 30 ºC, it has a blue color; As the temperature increases, the color transitions to a light purple; Further increase in temperature above 40 ºC results in purple color. In addition, the color-changing temperature of each dye is distinct, ranging from 30 °C for blue-violet to 68 °C for black-colorless. Such difference in the critical color-changing temperature of various dyes allows for integrating multiple types of dyes into the same structure for multi-color-changing purposes, which will be demonstrated and discussed later.

In addition, we explore the effect of adding thermochromic dye particles on the microstructure, and on thermal and mechanical properties of LCEs. **Figure 2B** presents scanning electron microscope (SEM) images (image I and II) of the cross-sectional area of two samples: pristine LCE and LCE embedded with red-colorless dye. Image I shows the relatively smooth surface of the pristine LCE film, while image II illustrates the relatively uniform distribution of the dye, represented by dots, in the LCE. Differential Scanning Calorimetry (DSC, Q20, TA Instruments) is employed to investigate the thermal-mechanical characteristics of pristine and thermochromic LCE films, as shown in **Figures 2C and D**. The comparison between the pristine LCE and LCE embedded with the blue-violet dye in Figure 2C reveals that adding the thermochromic dye to LCEs does not have a significant influence on the glass transition (T_g) and nematic-isotropic transition (T_{NI}) temperatures. The intense endothermic peak found in the DSC curve for the LCE embedded with blue-violet dye at around 30°C represents the color transition,

which is only observed in the thermochromic LCE film. Figure 2D shows the DSC curves of pristine LCE and thermochromic LCE films embedded with four different thermochromic dyes (black-colorless, blue-violet, black-green, and red-colorless), where each thermochromic film exhibits a different color transition temperature. **Figure S1** also shows the color transition temperature of pure dyes based on DSC testing, which are consistent with those in Figure 2D. Furthermore, engineering stress-strain curves of pristine and thermochromic LCE films (25 mm × 5 mm × 0.8 mm) are collected by performing dynamic mechanical analysis (DMA, Q800, TA Instruments) at a strain rate of 5%/min at 25°C. **Figure 2E** indicates that the addition of thermochromic dyes does not cause any significant effect on the mechanical properties and fracture limit of these materials. Even with the incorporation of thermochromic dyes, the LCE films remain very soft and stretchable, with the fracture strain close to 190% for pristine LCEs and LCEs embedded with dyes. The Young's modulus is further determined from the slope of the linear regime of the stress-strain curves (from 0% to 2% of strain, **Figure S2**). Although there are some slight variations in the moduli of LCEs embedded with different dyes, they generally remain very soft (~0.1-0.14 MPa) (**Figure 2F**). The moduli as a function of temperature for LCEs and LCEs with the red-colorless dyes are also characterized (**Figure S3**).

2.3 Reconfigurable, multi-color-changing biomimetic 3D thermochromic LCE structures

The color-changing properties in a variety of thermochromic dyes presented in Section 2.2 offer a potential opportunity for the realization of complex color transitions in biomimetic structures. For example, adding two thermochromic dyes (red-colorless dye and black-colorless dye) to the pristine LCE can enable reversible red-colorless and black-colorless transitions respectively at their respective color-changing temperatures: 52 ºC for red-colorless and 71 ºC

for black-colorless. Patterning the thermochromic LCE film into a butterfly-like geometry followed by compressive buckling forms a 3D butterfly-like structure, as shown in **Figure 3A**. Heating the structure above 52 ºC completes the red-colorless transition to simulate the process of a color-changing butterfly. Further heating the structure above 62 ºC enables the nematic-isotropic transition of LCEs, thereby morphing the 3D structure into its 2D configuration. The shape-switching process is also accompanied with the black-colorless transition when the temperature is above 71 ºC, realizing the colorless (the color of the pristine LCE) butterfly-like 2D pattern. The dynamic shape-switching and color-changing processes are recorded in **Movie S1**. Furthermore, by adding a third thermochromic dye of blue-violet, we develop thermochromic LCEs that can achieve three color transitions. **Figure 3B** and **Movie S1** show a chameleon-like structure assembled from the 2D pattern of thermochromic LCEs embedded with these three types of color-changing dyes. During the reconfiguration of the structure from the 3D shape to 2D pattern, the color transition is successive upon temperature increase: first experiencing blue-violet color change, followed by red-colorless and black-colorless color transitions, resembling the behaviors of color change and morphological reconfiguration of living organisms in nature[65, 66].

2.4 Underwater reconfigurable, color-changing 3D thermochromic LCE structures

The biomimetic camouflage strategy based on color-changing and shape-switching of thermochromic 3D biomimetic structures also has potential applications in underwater robotics. **Figure 4A** quantitatively shows the shape-morphing and color-changing behaviors of an "octopus" structure fabricated from LCE films embedded with red-colorless dye. The 3D shape of the "octopus" structure is prepared following the same strategy described above. To

characterize the shape-morphing and color-changing behaviors in underwater conditions, the structure is submerged in tap water and slowly heated and cooled across its nematic–isotropic transition temperature. Images from the side view of the sample are taken every 5 °C and used to measure the change in the length of the octopus's structure: the distance between the extremities of two tentacles with the largest lateral separation, as labeled in Figure 4a. Under room temperature (25 ºC), the structure is in the as-fabricated shape of an "octopus" in red color. As the temperature increases to 45 ºC, which is above the color-changing temperature of red dyes, the red color starts to disappear, while the structure maintains the shape of an "octopus" because it is still below the nematic-isotropic transition temperature of LCEs. As temperature further rises, the structure that is already in the colorless state also shows a gradual increase in length due to the shape-changing behavior that occurs at the nematic–isotropic transition temperature. Upon cooling, reversible shape-morphing and color-changing behaviors are observed. The heating-cooling process causes the reconfiguration between 2D and 3D mimicking the opening and close of the tentacles of an octopus, along with color changes. The plot in Figure 4a shows that the length of the structure changes reversibly with temperature, starting with 17.33 mm at 25 °C and achieving the maximum length of 18.96 mm at 75 °C. Additionally, **Figure 4B** compares the configurations of thermally induced color-changing and shape-morphing LCE structures to the swimming/camouflage states of an octopus in nature. At 25 °C, below the transition temperature of the red-colorless dye and the nematic-isotropic transition temperature of LCEs, the LCE structure presents a state of a red, swimming octopus, whereas the LCE structure at 80 °C transitions to the 2D, colorless configuration, mimicking the camouflage state of an octopus.

2.5 Ferromagnetic, thermochromic LCE robot for underwater applications

The reversible shape-switching and color-changing properties of thermochromic LCEs are promising for mimicking a variety of creatures in complex environments, such as the "flower", "butterfly", "chameleon" and "octopus" structures discussed in the sections above. By incorporating other functional elements like magnetic particles, we further develop a magnetically actuated thermochromic LCE robot, which endows the robot with multiple motion modes and thermos-magnetic dual responsiveness as shown in **Figure S4** and **Figure 5**. To enable the magnetic responsiveness of thermochromic LCEs, 10 vol% neodymium–iron–boron (NdFeB, MQFP-B-2007609-089, Neo Magneuench) microparticles with an average diameter of 5 μm are homogeneously embedded within thermochromic LCEs during its synthesis (see the experimental section for more details). The integration of magnetic particles has exhibit no significant influence on the shape-switching capability of LCEs as reported in our previous work[56]. Figure S4 shows the shape-morphing and color-changing behaviors of an "octopus" robot fabricated from the ferromagnetic thermochromic (black-green dye) LCE film, which can achieve multiple motion modes, including swimming, rolling, slippage, rotating, and crawling, under thermal and magnetic actuation. To minimize the influence of the black magnetic particles on the color change of LCEs as shown in Figure S4, we fabricated a bilayer structure composed of a thermochromic (red-colorless dye) LCE layer (325 μm) and a magnetic LCE layer (435 μm thick), as shown in **Figure 5A and Movie S2**. Compared to the single layer thermochromic magnetic LCE, the bilayer structure can achieve a better contrast of color changes in addition to the shape-morphing behaviors. **Movie S2** shows the top layer of the structure first changes its color from red to colorless above 52 ℃. Further increase in temperature above 62 ℃ induces the shape-morphing behavior due to the nematic-to-isotropic transition of LCEs.

We further demonstrate the "adaptive" motion enabled by the shape-morphing behavior of the structure. To enable more precise magnetic control, an impulse magnetizer (ASC scientific, IM-10-30) is used to magnetize the 3D structure along the horizontal (x-axis) direction. Under a 25 ℃ water environment, the structure is 3D and cannot be actuated via a magnet placed at a distance of d1=13 mm from the edge of the beaker, as shown in Figure 5B-I. When the temperature increases to 85 ℃, the structure morphs to 2D, which can move towards the magnet under the same magnetic control (**Movie S3**). In addition, Figure 5B shows that by morphing from 3D to 2D, the locomotion of the structure is faster, with the average speeds for 3D and 2D structures being 87.5 mm/s and 60.9 mm/s, respectively (**Movie S4**).

We also show the advantage of the thermo-magnetic dual responsiveness in the bilayer LCE structure, which is magnetized in the vertical (y-axis) direction. The 3D "octopus" structure can achieve various motion modes, including underwater locomotion, flipping, and swimming to the water surface, and camouflage under thermal and magnetic control. In addition, the red color of the structure blends well into the bright-color water environment at 25 ℃, which provides great camouflage (**Movie S5**). After heating to 85 ℃, the 3D octopus structure becomes 2D and cannot stay at the water surface, thereby slowly moving to the bottom of the water and achieving the camouflage in the relatively dark environment. The thermo-magnetic dual responsiveness allows the various motion modes and camouflage at different temperatures and locations.

3. Conclusion

In summary, the work presented here provides a facile and versatile strategy for realizing reversible shape-morphing and color-changing 3D thermochromic LCE structures synchronously.

Structures with large, reversible shape-switching and simultaneous color-changing behaviors illustrate the basic ideas and validate the concept. Four types of thermochromic dyes endow these structures with rich color transitions. Stress-strain and DSC curves demonstrate that the addition of dye particles has almost no influence on the properties of LCEs. Demonstrations of developed reconfigurable thermochromic biomimetic structures, including "butterfly" and "chameleon", highlight the feasibility of integrating shape-switching and multiple color-changing dye types in a single 3D structure, thereby enabling camouflage capabilities. In addition, the camouflage of an "octopus" structure further demonstrates that the strategy is applicable to the underwater condition, and the addition of ferromagnetic particles enables the magnetic response of "octopus", thereby achieving multiple biomimetic motion modes (swimming, rolling, slippage, rotating, and crawling), accompanied by color camouflage. Future work includes integrating electronic sensors into these reconfigurable thermochromic 3D LCE mesostructures to allow for synchronous actuation, sensing, and somatic control for a new generation of soft camouflage/reconnaissance robots and multifunctional bionic devices/systems.

Experimental Section

***Synthesis of thermochromic LCE Films*:** The LCE samples were synthesized following the two-stage thiol-acrylate Michael addition-photopolymerization (TAMAP)[60]. The tetra-functional thiol crosslinking monomer, the di-thiol spacer monomer, the photoinitiator, the catalyst and the solvent (2,2-(ethylenedioxy) diethanethiol (EDDET), pentaerythritol tetrakis(3-mercaptopropionate) (PETMP), (2-hydroxyethoxy)-2-methylpropiophenone (HHMP), dipropylamine (DPA) and toluene, respectively) were purchased from Sigma Aldrich and used as received. In addition, the di-acrylate mesogen, 4-bis-[4-(3-acryloyloxypropypropyloxy)

benzoyloxy]-2-methylbenzene (RM257), was purchased from Wilshire Technologies Inc. and used as received without any additional purification. 4 g of RM257 was dissolved in 1.6 g of toluene in a vial, which was then placed in an oven at 80 °C for around 10 min. After the RM257 was completely dissolved and cooled down to room temperature, 0.9157 g of EDDET and 0.2166 g of PETMP with a molar ratio of 85:15 were added to the solution. Consequently, 0.0257 g of HHMP, the photoinitiator that allows the second-stage reaction, was added to the solution, and then dissolved inside an oven at 80 °C following the same steps described above. After the complete dissolution of HHMP, 0.5680 g of a previously prepared solution of DPA in toluene with a mass ratio of 1:50, was added to the solution at room temperature, which was subsequently mixed for 1 min and defoamed for 2.5 min using a mixer (AR-100, Thinky) at 2000 rpm. The solution was then transferred to a high-density polyethylene (HDPE) mold to form LCE films of about 0.5-0.8 mm thick. The samples were cured at room temperature for 12 h and then placed in a vacuum oven at 80 °C and -0.68 bar for additional 24 h to completely remove the solvent.

To prepare thermochromic LCE films, four different colors of thermochromic dyes, black-colorless, blue-violet, black-green and red-colorless, were purchased from Atlanta Chemical and used as received. 0.2 g of the respective thermochromic dye was added into the solution after the addition of DPA. The remaining steps are the same as those for synthesizing pristine LCE films described above.

Similarly, the ferromagnetic LCE was prepared adding 10 wt% of neodymium–iron–boron (NdFeB, MQFP-B-2007609-089, Neo Magneuench) microparticles with an average diameter of

5 μm into the oligomer solution after the addition of DPA. The bilayer thermochromic ferromagnetic LCE film (760 μm thick in total) was prepared by adding thermochromic red-colorless LCE solution onto the top surface of a semi-cured ferromagnetic LCE layer (425 μm thick). After the addition of this second layer, the bilayer film was fully cured following the same steps described above.

***Tensile and compressive buckling of 3D LCE structures*:** With a CO_2 laser (VLS 2.30, Universal Laser System, Norman, CT), the LCE films were patterned into desired geometries and then laminated onto a soft silicone elastomer substrate (Dragon Skin; Smooth-On, Easton, PA) as an assembly platform. A thin layer of superglue was applied between the LCE pattern and the substrate at selective locations (bonding sites) to create strong bonding. For tensile buckling, stretching the elastomer substrate induced tensile forces at the bonding sites and transformed the 2D patterns into 3D structures. For compressive buckling, the 2D LCE patterns were laminated onto the prestretched elastomer substrate (Dragon Skin; Smooth-On, Easton, PA), with a thin layer of superglue applied between the pattern and the substrate at selective locations to create the bonding sites. Releasing the prestrain in the substrate induced compressive forces at the bonding sites and geometrically transformed the 2D pattern into a 3D structure. The permanent configuration was obtained by exposing the buckled 3D LCE structures for 8 min under UV light (wavelength: 365-400 nm), where the ordered monodomain was programed and the samples were locked into their 3D configurations. Heating above their nematic–isotropic transition temperature caused their reconfiguration to the 2D state.

Color changing of thermochromic LCE Films: LCE films embedded with different colors of thermochromic dyes (black-colorless, blue-violet, black-green and red-colorless) were laminated onto a glass slide and submerged inside a beaker containing tap water at room temperature. A hot

plate was used to gradually heat the tap water to temperatures above the color transition temperatures, while the color changes were evaluated.

Differential Scanning Calorimetry (DSC): DSC data was collected using a TA Instruments Q20 machine to determine the glass transition (T_g), color transition, and nematic-isotropic transition (T_{NI}) temperatures of pristine LCE and thermochromic LCE films embedded with different thermochromic dyes (black-colorless, blue-violet, black-green, and red-colorless). Samples of around 10 mg were loaded into standard aluminum DSC pans and placed inside the machine oven. First, the samples were heated from -60 °C to 150 °C at with a rate of 20 °C/min, equilibrated at 150 °C for 20 min to release any solvent or humidity that might be present, and in sequence cooled to -60 °C at 5 °C/min. Second, the samples were slowly heated and cooled between -60 °C and 150 °C at a rate of 5 °C/min to enable the LCE self-assembly. Finally, to obtain the transition temperatures, the samples were heated again from -60 °C to 150 °C at 5 °C/min. The glass transition temperatures (T_g) were measured at the shift of the baseline at low temperatures (~0-4 °C), and the nematic-isotropic transition temperatures (T_{NI}) were identified at the minimum value of the broad endothermic peak at high temperatures (~80-90 °C). Furthermore, the color transition temperature was also obtained at the minimum of the intense endothermic peak found from 30 °C to 70 °C in the DSC curves of thermochromic LCE films. Likewise, the DSC data of the pure thermochromic dyes (black-colorless, blue-violet, black-green, and red-colorless) were collected using around 4 mg of each dye, where the samples were heated from -50 °C to 100 °C at a rate of 10 °C/min, equilibrated at 100 °C for 5 min, cooled to -50 °C at 2 °C/min, and then heated again to 100 °C with a rate of 20 °C/min.

***Scanning Electron Microscope (SEM) imaging*:** The Teneo LV SEM was used to image the cross-sectional area of two samples, LCE embedded with red-colorless dye and pristine LCE, at

500x magnification using a low vacuum mode and LVD detector with a voltage of 10.00 kV and current of 0.40 nA.

Mechanical testing of pristine and thermochromic LCE Films: LCE samples embedded with different colors of thermochromic dyes (blue-violet, black-green and red-colorless) and pristine LCE samples were patterned into a dimension of 25 mm × 5 mm × 0.8 mm using a CO_2 laser (VLS 2.30, Universal Laser System, Norman, CT). Dynamic mechanical analysis (DMA) was then used in the tensile mode to test the patterned LCE samples at a displacement rate of 5% strain/min from 0 to 200% at 25°C.

Shape-changing behavior of the octopus structure: The 3D "octopus" structure prepared with the red-colorless dye was fixed inside a beaker containing tap water at room temperature. The beaker was covered with a parafilm and then slowly heated using a hot plate. Photos from the side view of the structure were taken at each 5 °C from 25 to 80 °C and consequently from 80 to 25 °C, when the hot plate was turned off and the tap water started to cool due to the temperature exchange with the environment. Furthermore, the change in length, which was considered as the distance between the two extremities of the two tentacles with the largest lateral separation, was calculated using the software ImageJ.

Fabrication and actuation of an underwater bilayer ferromagnetic-thermochromic LCE robot: The obtained bilayer thermochromic ferromagnetic LCE film (760 μm thick) was further patterned into the 2D "octopus" geometry. By using the 3D compressive buckling, a bio-inspired "octopus" robot was developed, which can synchronously respond to thermal stimuli and magnetic actuation. The color-changing of this thermochromic "octopus" robot was governed by the water temperature. For the magnetic actuation, an axially magnetized cylinder neodymium magnet (D8Y0, K&J magnetics) was used to actuate the "octopus" for its distinct motion modes,

including swimming, rolling, slippage, rotating and crawling. The strength and the direction of the applied magnetic field were adjusted via changing the distance and the angle between the circular magnet and the robot.

Acknowledgements

The authors acknowledge the support from the Office of Naval Research (N00014-19-1-2688). In addition, this work made use of the characterization facilities at the Institute of Materials Science at the University of Connecticut.

REFERENCES

1. L. Talas, R. J. Baddeley and I. C. Cuthill, *Philosophical Transactions of the Royal Society B: Biological Sciences*, 2017, **372**, 20160351.
2. R. C. Duarte, A. A. V. Flores and M. Stevens, *Philosophical Transactions of the Royal Society B: Biological Sciences*, 2017, **372**, 20160342.
3. R. Hanlon, *Current Biology*, 2007, **17**, R400-R404.
4. L. Phan, R. Kautz, E. M. Leung, K. L. Naughton, Y. Van Dyke and A. A. Gorodetsky, *Chemistry of Materials*, 2016, **28**, 6804-6816.
5. T. Bu, T. Xiao, Z. Yang, G. Liu, X. Fu, J. Nie, T. Guo, Y. Pang, J. Zhao, F. Xi, C. Zhang and Z. L. Wang, *Advanced Materials*, 2018, **30**, 1800066.
6. J. Byun, Y. Lee, J. Yoon, B. Lee, E. Oh, S. Chung, T. Lee, K.-J. Cho, J. Kim and Y. Hong, *Science Robotics*, 2018, **3**, eaas9020.
7. C. Larson, B. Peele, S. Li, S. Robinson, M. Totaro, L. Beccai, B. Mazzolai and R. Shepherd, *Science*, 2016, **351**, 1071-1074.
8. A. Morin Stephen, F. Shepherd Robert, W. Kwok Sen, A. Stokes Adam, A. Nemiroski and M. Whitesides George, *Science*, 2012, **337**, 828-832.
9. C. Laschi, B. Mazzolai and M. Cianchetti, *Science Robotics*, 2016, **1**, eaah3690.
10. H. Kim, H. Lee, I. Ha, J. Jung, P. Won, H. Cho, J. Yeo, S. Hong, S. Han, J. Kwon, K.-J. Cho and S. H. Ko, *Advanced Functional Materials*, 2018, **28**, 1801847.
11. P. Li, Y. Wang, U. Gupta, J. Liu, L. Zhang, D. Du, C. C. Foo, J. Ouyang and J. Zhu, *Advanced Functional Materials*, 2019, **29**, 1901908.
12. M. Stevens and S. Merilaita, *Philosophical Transactions of the Royal Society B: Biological Sciences*, 2009, **364**, 481-488.
13. S. Merilaita and J. Lind, *Proceedings of the Royal Society B: Biological Sciences*, 2005, **272**, 665-670.

14. H. M. Schaefer and N. Stobbe, *Proceedings of the Royal Society B: Biological Sciences*, 2006, **273**, 2427-2432.
15. M. Moirangthem and A. P. H. J. Schenning, *ACS Applied Materials & Interfaces*, 2018, **10**, 4168-4172.
16. H. Zhu, Q. Li, C. Tao, Y. Hong, Z. Xu, W. Shen, S. Kaur, P. Ghosh and M. Qiu, *Nature Communications*, 2021, **12**, 1805.
17. M. Pan, Y. Huang, Q. Li, H. Luo, H. Zhu, S. Kaur and M. Qiu, *Nano Energy*, 2020, **69**, 104449.
18. H. Zhu, Q. Li, C. Zheng, Y. Hong, Z. Xu, H. Wang, W. Shen, S. Kaur, P. Ghosh and M. Qiu, *Light: Science & Applications*, 2020, **9**, 1-8.
19. T. L. Williams, S. L. Senft, J. Yeo, F. J. Martín-Martínez, A. M. Kuzirian, C. A. Martin, C. W. DiBona, C.-T. Chen, S. R. Dinneen, H. T. Nguyen, C. M. Gomes, J. J. C. Rosenthal, M. D. MacManes, F. Chu, M. J. Buehler, R. T. Hanlon and L. F. Deravi, *Nature Communications*, 2019, **10**, 1004.
20. H. Kim, J. Choi, K. K. Kim, P. Won, S. Hong and S. H. Ko, *Nature communications*, 2021, **12**, 1-11.
21. S.-U. Kim, Y.-J. Lee, J. Liu, D. S. Kim, H. Wang and S. Yang, *Nature materials*, 2022, **21**, 41-46.
22. N. Ossi, B. S. Lekshmi, B. José Carlos, C. C. João, E. S.-S. Nicholas, K. V. Janne and B. Zbyszek, *Journal of Vertebrate Biology*, 2020, **69**, 20007.20001.
23. R. T. Hanlon, A. C. Watson and A. Barbosa, *The Biological Bulletin*, 2010, **218**, 15-24.
24. N. A. Traugutt, D. Mistry, C. Luo, K. Yu, Q. Ge and C. M. Yakacki, *Advanced materials (Deerfield Beach, Fla.)*, 2020, **32**, e2000797-e2000797.
25. E. C. Davidson, A. Kotikian, S. Li, J. Aizenberg and J. A. Lewis, *Advanced materials (Deerfield Beach, Fla.)*, 2020, **32**, e1905682-e1905682.
26. Q. He, Z. Wang, Y. Wang, A. Minori, M. T. Tolley and S. Cai, *Science advances*, 2019, **5**, eaax5746-eaax5746.
27. T. Guin, M. J. Settle, B. A. Kowalski, A. D. Auguste, R. V. Beblo, G. W. Reich and T. J. White, *Nature Communications*, 2018, **9**, 2531-Article No.: 2531.
28. A. Kotikian, R. L. Truby, J. W. Boley, T. J. White and J. A. Lewis, *Advanced materials (Deerfield Beach, Fla.)*, 2018, **30**.
29. J. Maeng, R. T. Rihani, M. Javed, J. S. Rajput, H. Kim, I. G. Bouton, T. A. Criss, J. J. Pancrazio, B. J. Black and T. H. Ware, *Journal of materials chemistry. B*, 2020, **8**, 6286-6295.
30. H. Shahsavan, A. Aghakhani, H. Zeng, Y. Guo, Z. S. Davidson, A. Priimagi and M. Sitti, *Proceedings of the National Academy of Sciences of the United States of America*, 2020, **117**, 5125-5133.
31. T. H. Ware, M. E. McConney, J. J. Wie, V. P. Tondiglia and T. J. White, *Science (Washington D C)*, 2015, **347**, 982-984.
32. M. O. Saed, A. H. Torbati, D. P. Nair and C. M. Yakacki, *Journal of Visualized Experiments*, 2016, 53546.
33. M. O. Saed, R. H. Volpe, N. A. Traugutt, R. Visvanathan, N. A. Clark and C. M. Yakacki, *Soft matter*, 2017, **13**, 7537-7547.

34. Z. Pei, Y. Yang, Q. Chen, E. M. Terentjev, Y. Wei and Y. Ji, *Nature materials*, 2014, **13**, 36-41.
35. M. J. Luo, S. S. Rao, Y. J. Tan, H. Yin, X. K. Hu, Y. Zhang, Y. W. Liu, T. Yue, L. J. Chen, L. Li, Y. R. Huang, Y. X. Qian, Z. Z. Liu, J. Cao, Z. X. Wang, Z. W. Luo, Y. Y. Wang, K. Xia, S. Y. Tang, C. Y. Chen and H. Xie, *Theranostics*, 2020, **10**, 3779-3792.
36. X. Liu, S.-K. Kim and X. Wang, *Journal of materials chemistry. B*, 2016, **4**, 7293-7302.
37. Y. Yang, W. Zhan, R. Peng, C. He, X. Pang, D. Shi, T. Jiang and Z. Lin, *Advanced materials (Deerfield Beach, Fla.)*, 2015, **27**, 6376-6381.
38. S.-k. Ahn, T. Ware, K. Lee, V. Tondiglia and T. White, *Abstracts of Papers American Chemical Society*, 2015, **250**, 433-433.
39. M. Barnes and R. Verduzco, *Soft Matter*, 2019, **15**, 870-879.
40. Z.-C. Jiang, Y.-Y. Xiao and Y. Zhao, *Advanced Optical Materials*, 2019, **7**, 1900262.
41. M.-H. Li, P. J. P. T. o. t. R. S. A. M. Keller, Physical and E. Sciences, 2006, **364**, 2763-2777.
42. H. Wermter and H. Finkelmann, *e-Polymers*, 2001, **1**.
43. D. K. Shenoy, D. L. Thomsen III, A. Srinivasan, P. Keller and B. R. Ratna, *Sensors and Actuators A: Physical*, 2002, **96**, 184-188.
44. Y. Zhang, Z. Wang, Y. Yang, Q. Chen, X. Qian, Y. Wu, H. Liang, Y. Xu, Y. Wei and Y. Ji, *Science advances*, 2020, **6**, eaay8606.
45. J. M. Boothby, J. C. Gagnon, E. McDowell, T. Van Volkenburg, L. Currano and Z. Xia, *Soft Robotics*, 2022, **9**, 154-162.
46. J. Liu, Y. Gao, H. Wang, R. Poling-Skutvik, C. O. Osuji and S. Yang, *Advanced Intelligent Systems*, 2020, **2**, 1900163.
47. Y. Huang, H. K. Bisoyi, S. Huang, M. Wang, X. M. Chen, Z. Liu, H. Yang and Q. Li, *Angew Chem Int Ed Engl*, 2021, **60**, 11247-11251.
48. Y. Wang, J. Sun, W. Liao and Z. Yang, *Advanced Materials*, 2022, **34**, 2107840.
49. H. Jiang, C. Li and X. Huang, *Nanoscale*, 2013, **5**, 5225-5240.
50. R. T. Rihani, H. Kim, B. J. Black, R. Atmaramani, M. O. Saed, J. J. Pancrazio and T. H. Ware, *Micromachines*, 2018, **9**, 416.
51. D. Tang, L. Zhang, X. Zhang, L. Xu, K. Li and A. Zhang, *ACS Applied Materials & Interfaces*, 2021.
52. J. Zhang, D. Sun, B. Zhang, Q. Sun, Y. Zhang, S. Liu, Y. Wang, C. Liu, J. Chen and J. Chen, *Materials Horizons*, 2022.
53. Y.-S. Zhang, S.-A. Jiang, J.-D. Lin and C.-R. Lee, *Journal of Materials Chemistry C*, 2020, **8**, 5517-5524.
54. B. Zuo, M. Wang, B.-P. Lin and H. Yang, *Chemistry of Materials*, 2018, **30**, 8079-8088.
55. H. Shahsavan, A. Aghakhani, H. Zeng, Y. Guo, S. Davidson Zoey, A. Priimagi and M. Sitti, *Proceedings of the National Academy of Sciences*, 2020, **117**, 5125-5133.
56. Y. Li, H. Yu, K. Yu, X. Guo and X. Wang, *Advanced Functional Materials*, 2021, **31**, 2100338.
57. K. Bašnec, L. S. Perše, B. Šumiga, M. Huskić, A. Meden, A. Hladnik, B. B. Podgornik and M. K. Gunde, *Scientific Reports*, 2018, **8**, 5511.
58. V. Durasevic, in *Advances in Smart Medical Textiles*, ed. L. van Langenhove, Woodhead Publishing, Oxford, 2016, pp. 19-55.
59. C. Ohm, M. Brehmer and R. Zentel, *Advanced Materials*, 2010, **22**, 3366-3387.

60. C. Yakacki, M. Saed, D. Nair, T. Gong, S. Reed and C. Bowman, *Rsc Advances*, 2015, **5**, 18997-19001.
61. M. Ecker and T. Pretsch, *RSC Advances*, 2014, **4**, 286-292.
62. C. Zhu and A. Wu, *Thermochimica acta*, 2005, **425**, 7-12.
63. H. Y. M. Ram and G. Mathur, *Journal of Experimental Botany*, 1984, **35**, 1656-1662.
64. Y. Teppabut, K.-i. Oyama, T. Kondo and K. Yoshida, *Molecules*, 2018, **23**, 1698.
65. A. E. Best, *Annals of Science*, 1968, **24**, 147-167.
66. J. Teyssier, S. V. Saenko, D. van der Marel and M. C. Milinkovitch, *Nature Communications*, 2015, **6**, 6368.

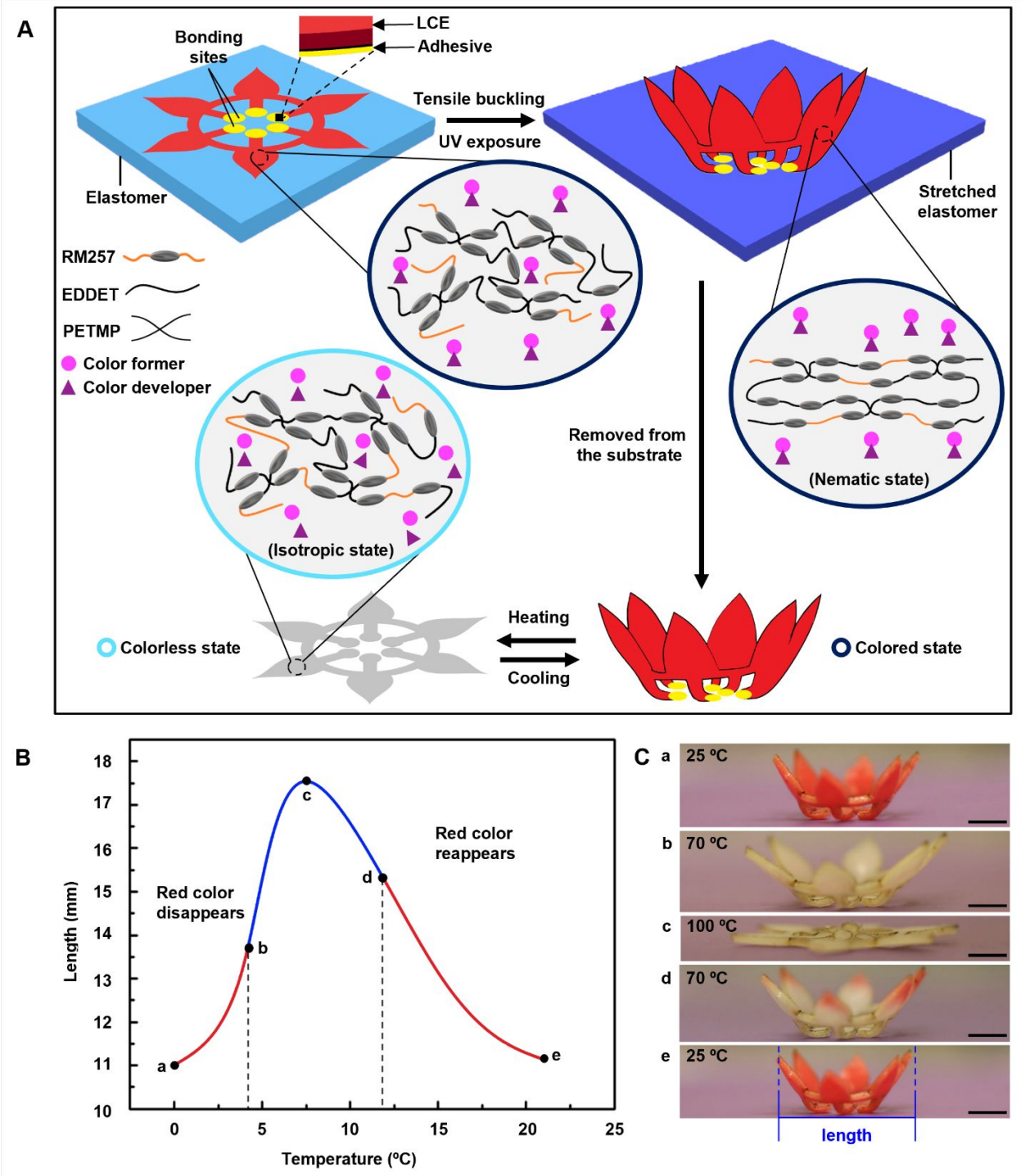

Figure 1. Thermochromic LCE structures with reversible, synchronous shape-morphing and color-changing capabilities. (**A**) Schematic illustration of the assembly and reconfiguration process of a thermochromic LCE structure with the associated microscale mechanisms for the programming of LC molecular orders and the state transition of thermochromic dyes. **(B)** Quantitative characterizations of the shape morphing and color changing of an assembled

thermochromic LCE structure that resembles a flower. **(C)** Optical images a-e corresponding to the points labelled in Figure 1B. Scale bars: 3 mm.

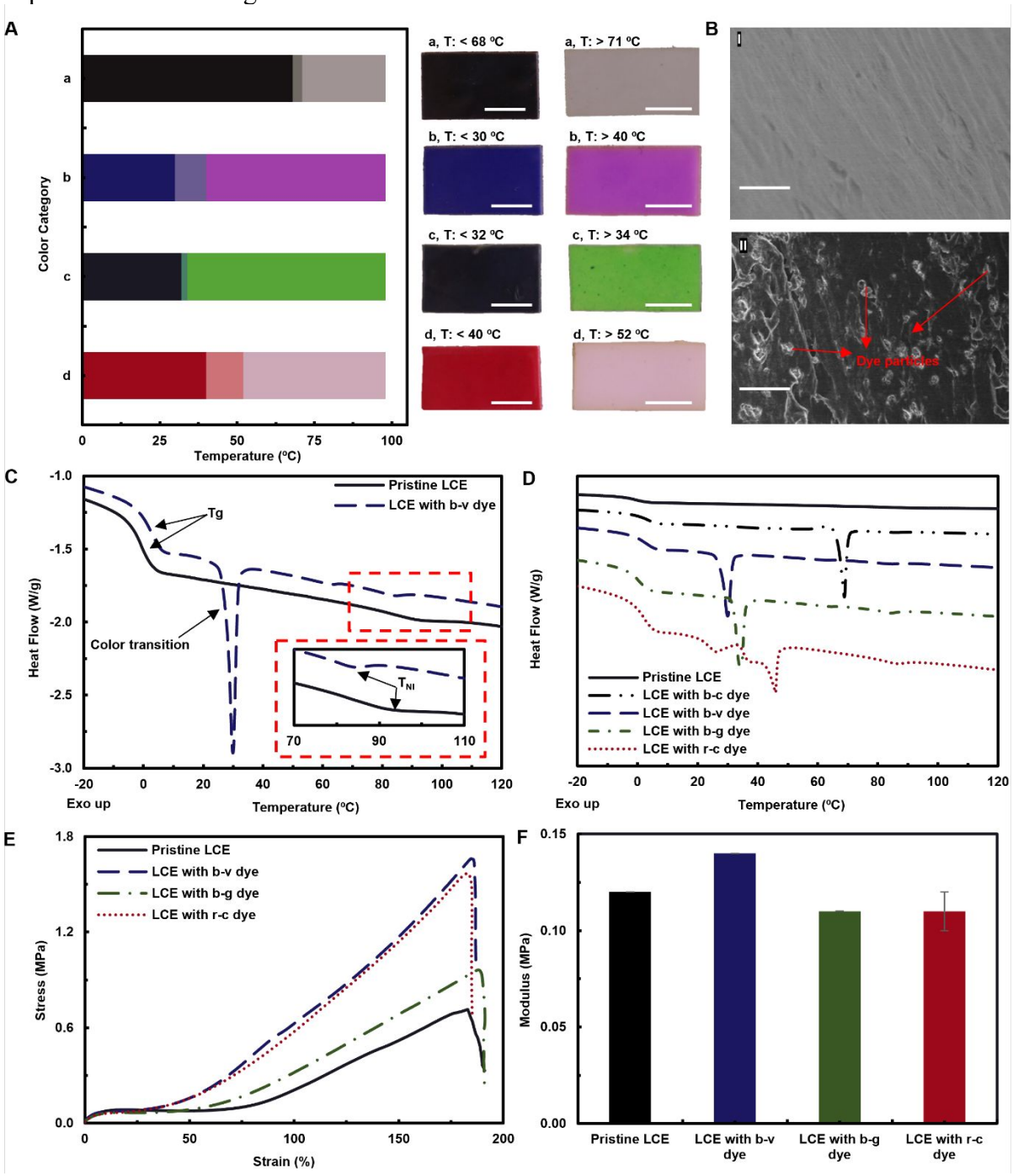

Figure 2. Characterizations of thermochromic LCEs. (**A**) The color-changing temperature of thermochromic LCE films embedded with different thermochromic dyes: (a) black-colorless, (b) blue-violet, (c) black-green, and (d) red-colorless. Scale bars: 3 mm. (**B**) SEM images of pristine LCE and thermochromic LCE films. Scale bars: 30 μm. (C) DSC curves of pristine LCE and thermochromic LCE (embedded with the blue-violet dye) films. (D) DSC curves of pristine LCE and thermochromic LCE films embedded with different types of dyes. Please note that the curves

are shifted for a better demonstration of the color transition temperature with different dyes. b-c, b-v, b-g, and r-c represent black-colorless, blue-violet, black-green, and red-colorless, respectively. (**E**) Engineering stress-strain curves of pristine LCE and thermochromic LCE films. (**F**) Elastic modulus of pristine LCE and thermochromic LCE films.

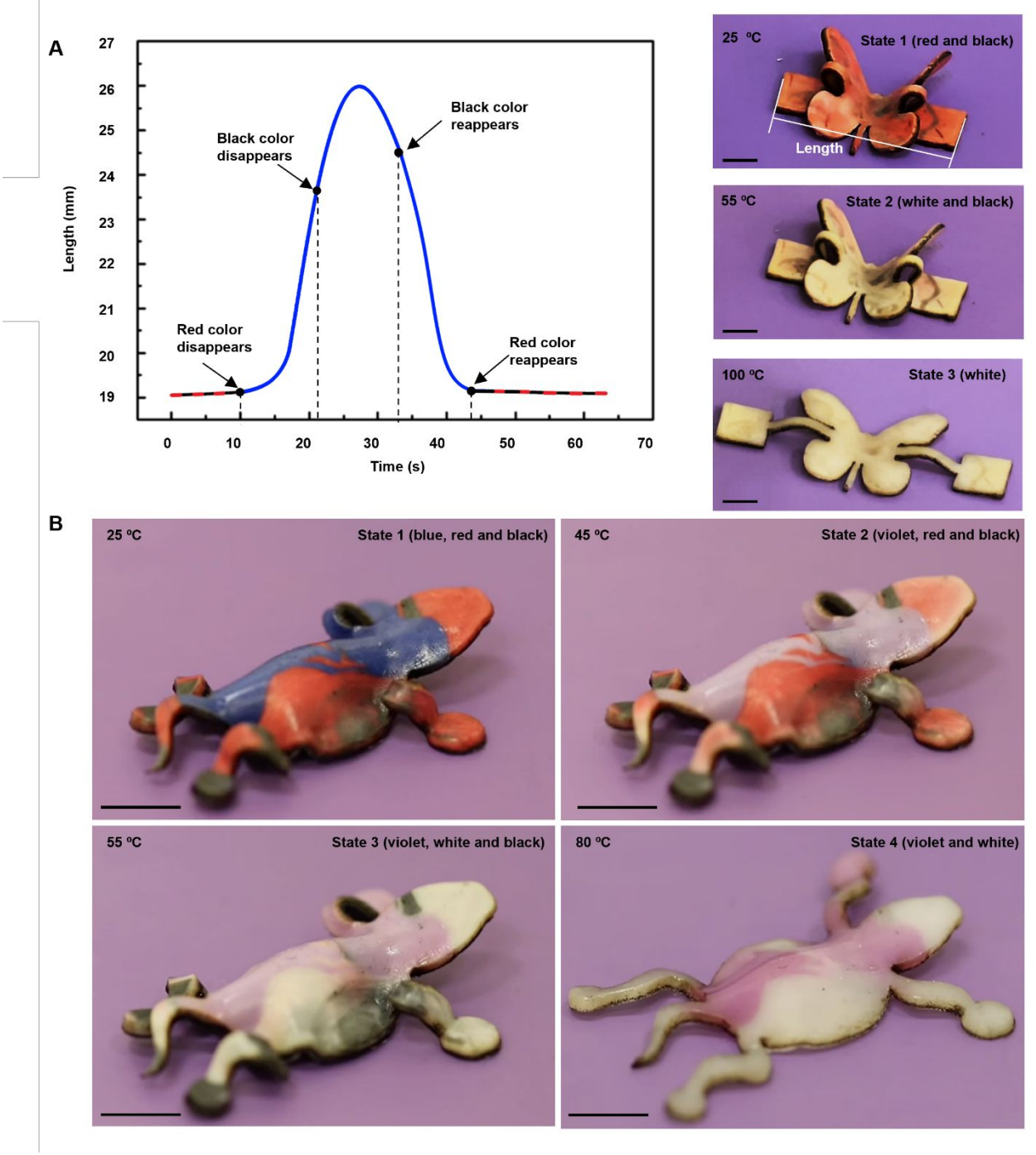

Figure 3. Reversibly reconfigurable and multi-color-changing thermochromic LCE structures. (**A**) Quantitative characterizations of the shape-morphing and multi-color-changing behaviors of a butterfly-like thermochromic LCE structure. Scale bars: 3 mm. (**B**) Optical images

of a chameleon-like structure with reversible shape-switching and three-color-changing behaviors: blue-violet, red-colorless, black-colorless. Scale bars: 3 mm.

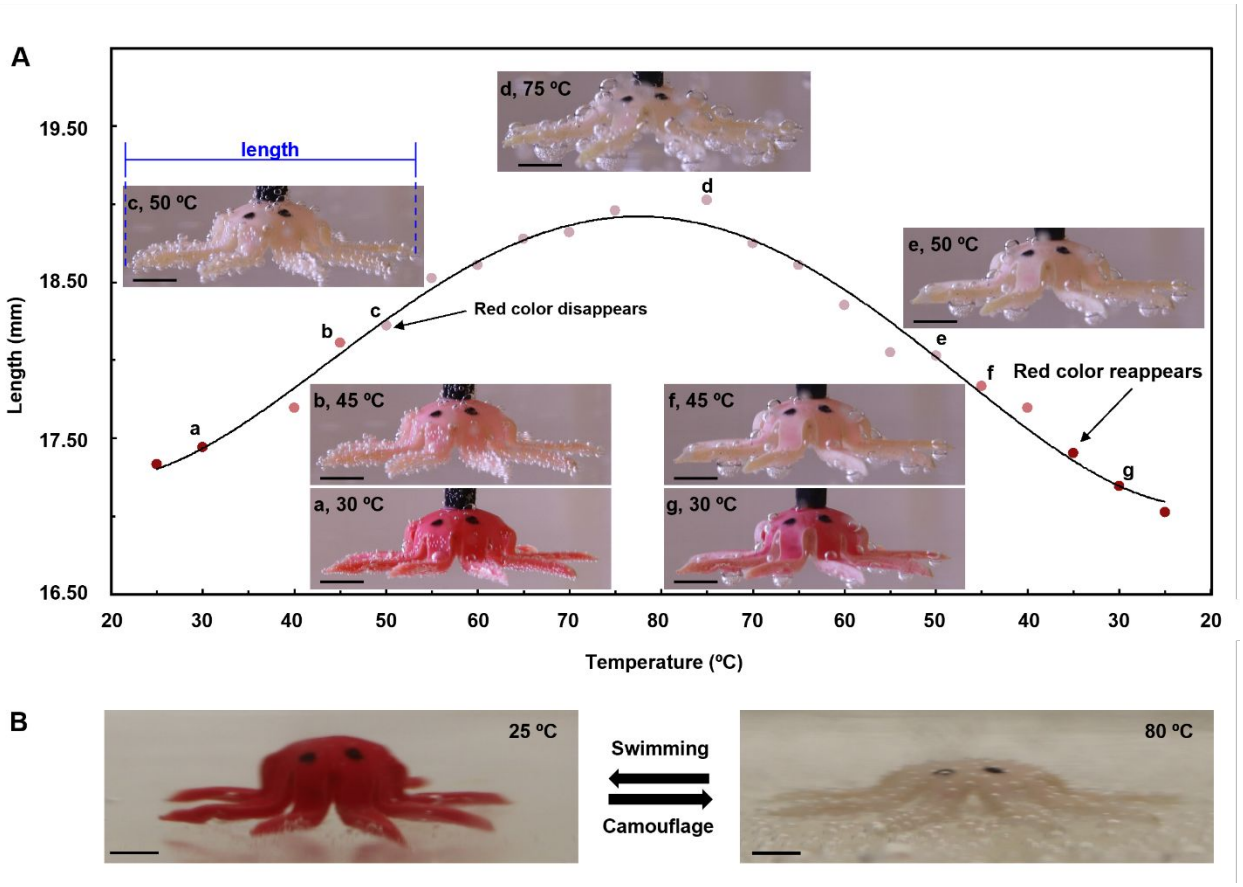

Figure 4. Underwater shape-morphing and color-changing "octopus" robot. (**A**) Shape changes of the octopus-like structure as a function of temperature, along with corresponding optical images of the structure at selective temperature. Scale bars: 3 mm. (**B**) Biomimicry of the "octopus" robot at high and low temperatures, corresponding to the swimming/camouflage states of an octopus in nature. Scale bars: 3 mm.

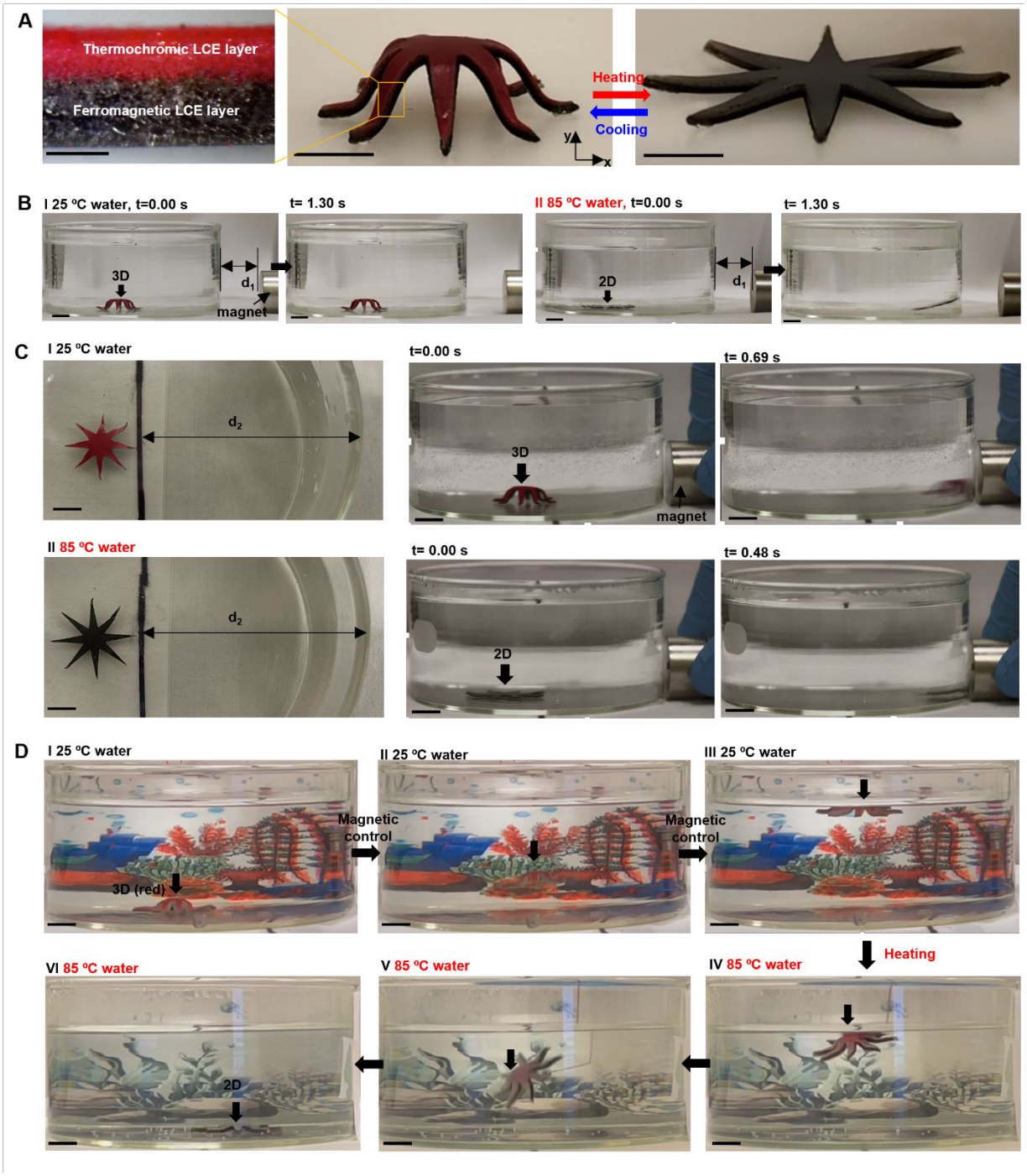

Figure 5. Bilayer thermochromic/magnetic LCE robot with shape-morphing and color-changing capabilities for underwater applications. (A) Optical images of a bilayer structure composed of thermochromic and ferromagnetic LCEs as well as its shape morphing and color changing behavior upon heating and cooling. Scale bars, 0.5 mm for the zoomed-in view; 5 mm for the images of 3D and 2D structures. (**B**) Magnetic actuation of a bilayer "octopus" structure at a water temperature of 25 ℃ (I) and 85 ℃ (II), respectively. d_1=13 mm. Scale bars, 5 mm. (**C**) "Adaptive" motion of the "octopus" structure when the water temperature changes from 25 ℃ to

85 ℃, under the same magnetic control. d_2=42 mm. Scale bars, 5 mm. (**D**) Various motion and camouflage behaviors of the "octopus" structure via thermo-magnetic dual responsiveness. Scale bars, 5 mm.